SPECIAL
Waves to Weather (W2W)
COLLECTION

Moist Thermodynamics of Convectively Coupled Waves over the Western Hemisphere

VÍCTOR C. MAYTA[a] AND ÁNGEL F. ADAMES[a]

[a]*Department of Atmospheric and Oceanic Sciences, University of Wisconsin–Madison, Madison, Wisconsin*

(Manuscript received 10 June 2022, in final form 21 December 2022)

ABSTRACT: Convectively coupled waves (CCWs) over the Western Hemisphere are classified based on their governing thermodynamics. It is found that only the tropical depressions (TDs; TD waves) satisfy the criteria necessary to be considered a moisture mode, as in the Rossby-like wave found in an earlier study. In this wave, water vapor fluctuations play a much greater role in the thermodynamics than temperature fluctuations. Only in the eastward-propagating inertio-gravity (EIG) wave does temperature govern the thermodynamics. Temperature and moisture play comparable roles in all the other waves, including the Madden–Julian oscillation over the Western Hemisphere (MJO-W). The moist static energy (MSE) budget of CCWs is investigated by analyzing ERA5 data and data from the 2014/15 observations and modeling of the Green Ocean Amazon (GoAmazon 2014/15) field campaign. Results reveal that vertical advection of MSE acts as a primary driver of the propagation of column MSE in westward inertio-gravity (WIG) wave, Kelvin wave, and MJO-W, while horizontal advection plays a central role in the mixed Rossby gravity (MRG) and TD wave. Results also suggest that cloud radiative heating and the horizontal MSE advection govern the maintenance of most of the CCWs. Major disagreements are found between ERA5 and GoAmazon. In GoAmazon, convection is more tightly coupled to variations in column MSE, and vertical MSE advection plays a more prominent role in the MSE tendency. These results along with substantial budget residuals found in ERA5 data suggest that CCWs over the tropical Western Hemisphere are not represented adequately in the reanalysis.

SIGNIFICANCE STATEMENT: In comparison to other regions of the globe, the weather systems that affect precipitation in the tropical Western Hemisphere have received little attention. In this study, we investigate the structure, propagation, and thermodynamics of convectively coupled waves that impact precipitation in this region. We found that slowly evolving tropical systems are "moisture modes," i.e., moving regions of high humidity and precipitation that are maintained by interactions between clouds and radiation. The faster waves are systems that exhibit relatively larger fluctuations in temperature. Vertical motions are more important for the movement of rainfall in these waves. Last, we found that reanalysis and observations disagree over the importance of different processes in the waves that occurred over the Amazon region, hinting at potential deficiencies on how the reanalysis represents clouds in this region.

KEYWORDS: Convection; Gravity waves; Madden–Julian oscillation; Atmospheric waves

1. Introduction

Precipitation over the tropical belt (~20°N/S) is organized over a wide range of spatial and temporal scales. Among the organized precipitation systems, we see mesoscale convective systems (MCSs), synoptic-scale convectively coupled waves (CCWs), and planetary-scale disturbances such as the Madden–Julian oscillation (MJO; Takayabu 1994; Wheeler and Kiladis 1999; Wheeler et al. 2000; Kiladis et al. 2009; Zhang et al. 2020).

Over the tropical Western Hemisphere, the MJO and equatorial Rossby-like waves act as major sources of intraseasonal precipitation variability (e.g., Mayta et al. 2019, 2022). At the weekly time scale, the convectively coupled Kelvin wave is one of the most well-researched synoptic-scale waves over tropical South America (Liebmann et al. 2009; Serra et al. 2020; Mayta et al. 2021). At the daily time scale, 2-day westward inertio-gravity waves (WIGs) have been shown to be organized as mesoscale convective systems over the Amazon (Silva Dias and Ferreira 1992; Mayta and Adames 2021). The impact of the other CCWs on precipitation, on the other hand, is less explored. Furthermore, there have been few efforts to compare how the different CCWs modulate Western Hemisphere rainfall.

A remaining challenge in our understanding of CCWs is our lack of understanding of the processes in which the large-scale tropical circulation interacts with deep convection (Neelin and Held 1987; Raymond 2001; Mapes et al. 2006; Kiladis et al. 2009; Wolding et al. 2022). It is well-known that free-tropospheric

Corresponding author: Víctor C. Mayta, mayta@wisc.edu

DOI: 10.1175/JCLI-D-22-0435.1

water vapor plays a key role in the occurrence and organization of tropical deep convection (Raymond 2001; Bretherton et al. 2004; Sobel et al. 2004; Mayta et al. 2022). It can also dominate the thermodynamic behavior of slowly evolving motions, leading to so-called moisture modes (Kim et al. 2014; Adames and Kim 2016; Adames and Maloney 2021). While the study of moisture modes has mostly focused on the Indo-Pacific warm pool (Raymond et al. 2009), a recent study by Mayta et al. (2022) showed evidence that equatorial Rossby-like waves in the Western Hemisphere may actually be moisture modes. However, it is unknown whether moisture modes are common systems in the tropics and if other systems in the Western Hemisphere may also exhibit moisture mode behavior.

Many researchers have invoked the moist static energy (MSE) budget to understand how convection and large-scale circulation interact since high values of MSE have been found to be associated with tropical convection (Inoue and Back 2015; Yasunaga et al. 2019). MSE also summarizes the thermodynamics of CCWs and the MJO (Sumi and Masunaga 2016; Adames et al. 2019; Ahmed et al. 2021). The MSE budget was widely used to explore the processes involved in the propagation and maintenance of the MJO (e.g., Maloney 2009; Kiranmayi and Maloney 2011; Andersen and Kuang 2012; Kim et al. 2014; Sobel et al. 2014; Hannah and Maloney 2014; Gonzalez and Jiang 2019; among others). The MSE budget has also been employed to study other CCWs over the Indo-Pacific warm pool (Inoue and Back 2015; Sumi and Masunaga 2016; Yasunaga et al. 2019; Inoue et al. 2020; Mayta et al. 2022). However, little work has been done to understand the MSE budget of systems that occur in the tropical Western Hemisphere.

The main goal of this study is to examine potential regional differences in the dynamics and thermodynamics of CCWs. We seek to answer the following questions:

1) What are the thermodynamic characteristics of CCWs in the tropical Western Hemisphere?
2) Is the MSE budget of CCWs in the tropical Western Hemisphere different from that of CCWs that occur over the warm pool?
3) What do these results tell us about the convective coupling of tropical waves? For instance, which behaves like moisture modes?

The paper is organized as follows: section 2 provides a brief description of the datasets and analysis methods. In section 3, we elucidate the horizontal structure of CCWs and their associated convection on the basis of a linear regression analysis. The governing thermodynamics for all disturbances are examined in section 5. In section 6, an MSE budget analysis is performed for each wave type. Finally, the major findings of the study are summarized in section 7.

2. Data and methods

a. CLAUS brightness temperature dataset

Satellite-observed brightness temperature T_b data are used as a proxy for tropical convection in this study. The data are obtained from the Cloud Archive User System (CLAUS) satellite data (Hodges et al. 2000), which has eight-times-daily global fields of T_b from July 1983 to June 2009 and extended through 2017 using the merged IR dataset from NOAA.

b. ERA5

To assess the dynamical and thermodynamical characteristics associated with CCWs, 4-times-daily atmospheric variables from the fifth major global reanalysis produced by the European Centre for Medium-Range Weather Forecasts (ERA5; Hersbach et al. 2019) are used. The ERA5 dataset we employed has a 0.5° horizontal resolution, with four-times-daily analyses that match the CLAUS T_b data for the 36-yr time period from 1984 through 2015. We make use of the zonal u, meridional v, and vertical ω winds, specific humidity q, temperature T, diabatic heating rate Q_1, surface and top-of-the-atmosphere radiative fluxes, surface sensible SH and latent heat fluxes L_vE, and precipitation P.

c. GoAmazon 2014/15 field campaign data

The observations and modeling of the Green Ocean Amazon (GoAmazon 2014/15) experiment were carried out in Manacapuru, in western Manaus in central Amazonia, Brazil, for the 2-yr time period from 1 January 2014 through 31 December 2015. GoAmazon 2014/15 consists of three main integrated components: a field campaign, data analysis, and modeling. The field campaign involved measures of complex interactions among vegetation, atmospheric chemistry, and aerosol production and their connections to clouds and precipitation [more details in Martin et al. (2016)]. For this study, we make use of the constrained variational analysis product for GoAmazon (VARANAL; Tang et al. 2016) to analyze the regional scale of the vertical dynamic and thermodynamic structure associated with the CCWs. VARANAL is derived from the ECMWF analysis fields and Atmospheric Radiation Measurement's (ARM's) observations during GoAmazon 2014/15 using the constrained variational analysis proposed in Zhang and Lin (1997). This product assimilates the top of the atmosphere and surface observations to produce thermodynamic budgets. The surface observations assimilated include surface radiative, latent, and sensible heat fluxes and precipitation from the System for the Protection of Amazonia (SIPAM) radar. Additional details about VARANAL products during GoAmazon 2014/15 are found in Tang et al. (2016).

d. Wave-type filtering of CLAUS T_b and EOF calculation

To isolate individual CCW modes, T_b is filtered following the method proposed by Wheeler and Kiladis (1999) using the same frequency–wavenumber boxes documented in Kiladis et al. (2009). This is accomplished in the wavenumber–frequency domain by retaining only those spectral coefficients within a specific range corresponding to the spectral peaks associated with a given mode. The filter settings for the period, the wavenumber k, and the equivalent depth h_e are detailed in Table 1.

Considering that filtered anomalies include background noise, we use empirical orthogonal function (EOF) analysis to

TABLE 1. Convectively coupled tropical waves with their corresponding characteristics. The filter settings for the period, wavenumber k, and the equivalent depth h_e used to extract the wave signal [see Kiladis et al. (2009) for more details]. Positive (negative) k corresponds to modes with eastward (westward) propagation. The variance explained by the two leading patterns (PC1 and PC2) is also shown in the last columns. The values for the Rossby-like wave come from Mayta et al. (2022).

Acronym	Wave	Period (days)	k	h_e (m)	PC1 (%)	PC2 (%)
WIG	Westward inertio-gravity	1.25 to 3.5	−15 to −1	12 to 90	7.8	7.7
EIG	Eastward inertio-gravity	1 to 6	0 to 15	12 to 50	8.1	6.0
KW	Kelvin wave	2.5 to 20	1 to 15	—	17.5	15.2
MRG	Mixed Rossby gravity	2.5 to 10	−10 to −1	8 to 90	8.4	7.8
TD-like	Tropical disturbance	2 to 10	−20 to −5	—	9.5	9.2
MJO-W	Western Madden–Julian oscillation	20 to 90	0 to +10	—	16.8	12.9
ER-like	Equatorial Rossby-like	10 to 90	−20 to 0	—	13.4	12.8

extract the dominant mode associated with each CCW mode. The EOF analysis is limited to the tropical Western Hemisphere (10°S–15°N, 120°W–0°), considering the maximum variance of CCWs shown in Fig. 1. Since T_b are filtered for either eastward or westward propagation, the EOFs occur in pairs and together account for the leading convective circulation pattern and propagation. In addition, the first two eigenvalues are close together and represent the sine and cosine parts of the wave, and they are well separated from the third eigenvalue based on the North et al. (1982) degenerate mode criteria.

e. Linear regression

The dynamical fields associated with each EOF of the corresponding CCWs are obtained by projecting raw T_b and ERA5 data at each grid point onto the associated principal component (PC) time series. Then, all fields are scaled to one standard deviation PC perturbation of the corresponding wave. The statistical significance of these results is then assessed based on a two-tailed Student's t test that takes into account the correlation coefficients and an effective number of independent sample (degrees of freedom) based on the decorrelation time scale (Livezey and Chen 1983). Similarly, the relationship between the CCW mode and MSE budget terms was determined by using linear regression, following the same procedure as previous studies (e.g., Mapes et al. 2006; Adames et al. 2021; Mayta et al. 2021; Snide et al. 2022).

3. Large-scale structure of the CCWs over the Western Hemisphere

a. WIG waves

The leading pair of PCs of T_b data filtered over the WIG band explain 15.6% of the total variance. Figure 2 shows T_b (shading), 850-hPa geopotential height (contours), and winds (vectors) for a WIG wave obtained from a linear regression of these fields onto the PC1 time series of WIGs. From day −1 (Fig. 2a) convection propagates westward from northeast South America and reaches the eastern slope of the Andes 2 days later with an arch-shaped structure (day +1; Fig. 2c). The low-level wind circulation is first dominated by convergent flow, which is shifted to the west of the convective center (Fig. 2b). This is the result of the tilted structure that has divergence aloft shifted to the east of the low-level convergence [see Figs. 5 and 6 in Mayta and Adames (2021)]. The convective and circulation features are similar to those documented in other regions such as the Indian Ocean (Takayabu et al. 1996; Haertel and Kiladis 2004) and western Pacific (Kiladis et al. 2009). The horizontal scale of the regressed waves approximately corresponds to zonal wavenumbers 8 and 9 (a wavelength of ~40°). A detailed study of the dynamic and thermodynamic features of the 2-day waves was documented in Mayta and Adames (2021).

b. EIG waves

Figure 1b represents the geographical distribution of the eastward inertio-gravity (EIG) wave–filtered T_b variance over

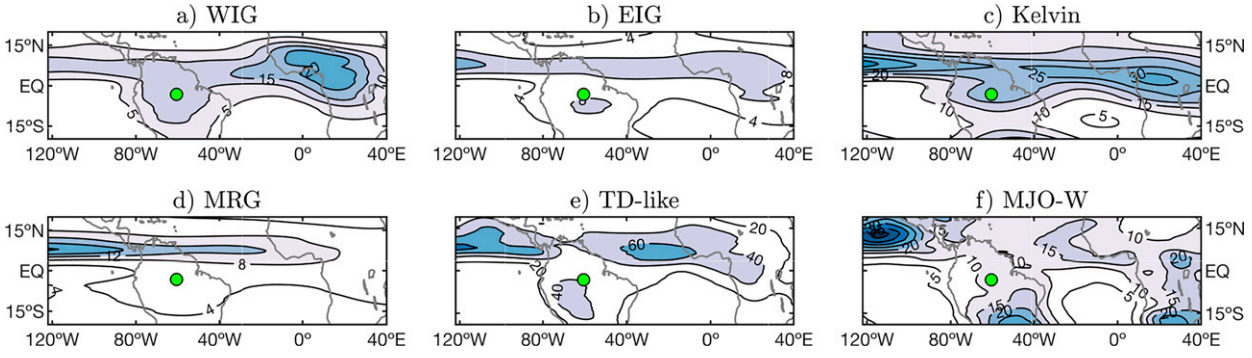

FIG. 1. Geographical distribution of the variance of CCW-filtered CLAUS T_b for all seasons. Shading intervals (in K^2) are shown in each panel. The location of the ARM T3 radiosonde station at Manacapuru (3.15°S, 60.6°W) is indicated by a green circle.

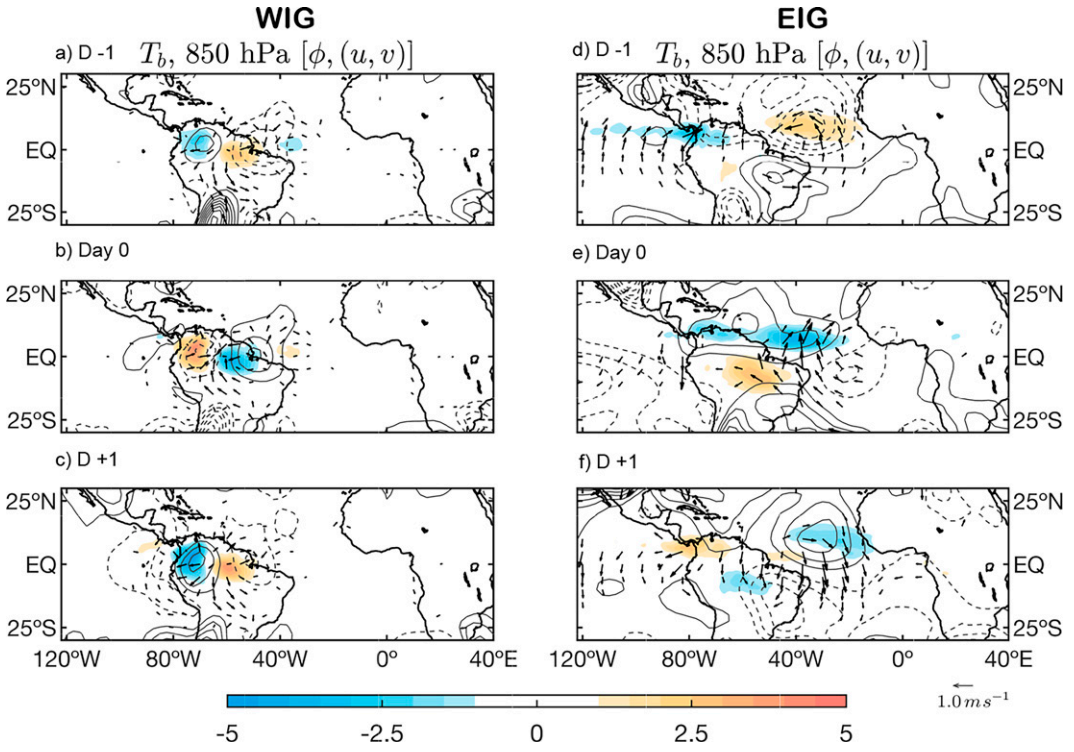

FIG. 2. Anomalous CLAUS T_b (shading), 850-hPa geopotential height (contours), and 850-hPa winds (vectors) regressed onto PC1 of the (left) WIG and (right) EIG from (top to bottom) day −1 through day +1. All fields are scaled to one standard deviation PC perturbation of the corresponding wave. Geopotential height contour interval is 2 m. Shading and contours indicate regions significant at the 95% level. Wind vectors are plotted only where either the u or v component is significant at the 95% level or greater.

all seasons. Since the EIG wave is defined to be antisymmetric in the T_b field, the maximum variance over the Western Hemisphere is off equatorial. While the EIG wave shows its maximum variance near the date line (Kiladis et al. 2009), a substantial signature is still seen in the Western Hemisphere, as seen in Figs. 2d–f. For EIGs, PC1 and PC2 together explain about 14% of the total variance of the high-frequency filtered band. EIGs are characterized by zonal wavelength that is nearly twice that of WIGs at ~75°. The EIG waves propagate faster than WIGs at about 32.5 m s^{-1}. The quadrupole structure in anomalous convection characteristic of EIGs is not as evident over the Western Hemisphere as it is over the tropical western Pacific [e.g., Fig. 17 in Wheeler et al. (2000)], even though the circulation at 850 hPa closely matches shallow-water theory.

c. *Kelvin waves*

For Kelvin waves, PC1 and PC2 together explain 32.7% of the filtered variance. Over the Western Hemisphere domain, Kelvin waves have a characteristic zonal wavenumber ~5 (a wavelength of ~75°) and propagate at a phase speed of 15.8 m s^{-1}. Convection associated with the Kelvin waves starts in the eastern Pacific at day −2 (Fig. 3a). As documented in previous studies (e.g., Liebmann et al. 2009; Mayta et al. 2021), anomalous convection over the tropical South American and Atlantic region is often excited by a preexisting Kelvin wave that propagates into the region from the eastern Pacific. Those studies also found that, in many instances, extratropical wave train activity triggers convection in the equatorial region, projecting onto large-scale Kelvin waves. Convection reaches the continental part on day 0 (Fig. 3b) and continues its eastward propagation in the following days. Winds at 850 hPa are easterly to the east of maximum Kelvin wave precipitation (day −2; Fig. 3a), and westerlies occur nearly in phase with enhanced precipitation. Equatorial zonal winds are in phase with pressure, resembling the theoretical Kelvin wave (Matsuno 1966), most evident at day +2 (Fig. 3c).

d. *MRG waves*

Figure 1d shows the geographical distribution of the mixed Rossby gravity (MRG) wave-filtered T_b variance for all seasons. The maximum activity of this wave is observed in the eastern Pacific and northern South America. Applying EOFs over the region maximum variance, we find that PC1 and PC2 together explain 16.2% of the total variance (Table 1). The horizontal structure of PC1 associated with the convectively coupled MRG wave for different time lags is shown in Figs. 4a–c. From here on we show the streamfunction, rather than the geopotential, as the contoured field since it more clearly depicts balanced equatorial circulations. Over the Western Hemisphere domain, the MRGs have an average zonal wavenumber between 4 and 5 (a wavelength of ~80°) and propagate at a phase speed

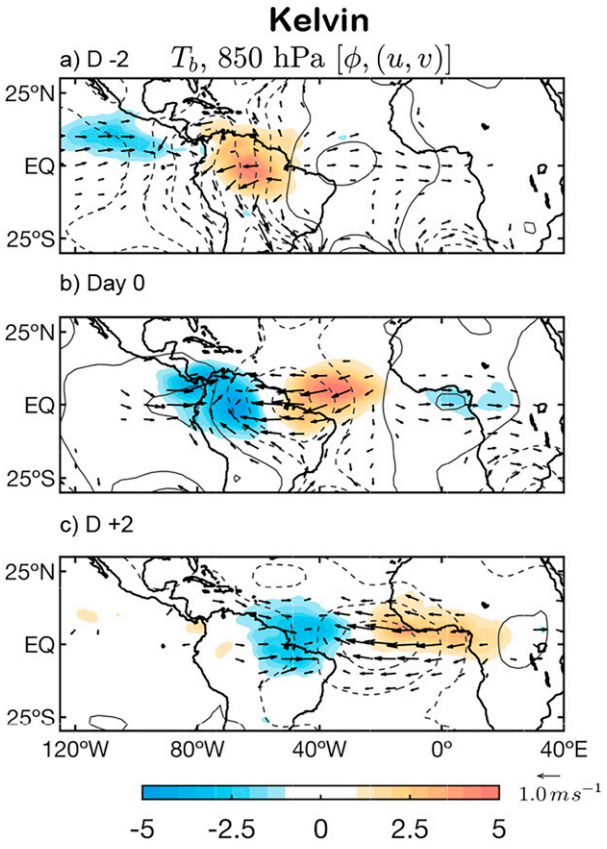

FIG. 3. As in Fig. 2, but for Kelvin waves for (a) day −2, (b) day 0, and (c) day +2. Geopotential height contour interval is 2 m.

of 19.5 m s^{-1}. Convection associated with MRG waves initially appears over northern South America (day −1; Fig. 4a) and propagates westward in the following days, showing its maximum amplitude at day 0 (Fig. 4b). In contrast with Kiladis et al. (2016), MRG convection over northern South America and the eastern Pacific propagates zonally rather than meridionally [see Fig. 6 in Kiladis et al. (2016)]. Convection is primarily located in the ITCZ in the Northern Hemisphere in contrast to the shallow-water MRG wave, which has convective anomalies in both hemispheres. On the other hand, the horizontal circulation is still similar to that expected from the theory and MRGs over the western Pacific (e.g., Wheeler et al. 2000; Kiladis et al. 2009, 2016). MRG waves of 850-hPa streamfunction are propagating westward through the region of convective activity. Although off-equatorial gyres can be expected as a response to heating (located mainly in the Northern Hemisphere), gyres are still symmetric with respect to the equator. Northerly low-level winds in phase with suppressed convection and southerly winds coupled with enhanced convection are observed in agreement with the MRG wave structure documented in Kiladis et al. (2009) and Kiladis et al. (2016).

e. TD-like waves

For tropical depression (TD)-like waves, PC1 and PC2 together explain 18.7% of the filtered variance and represent the TD wave activity over the western coast of Africa and the tropical Atlantic, in agreement with the geographical distribution of the maximum annual-mean TD variance (Fig. 1d). Figures 4d–f display the day −1 to day +2 evolution of T_b and 850-hPa circulation projected onto PC1 of the TD-like wave. The regressed TDs exhibit a zonal wavelength of 35° (zonal wavenumber ~10), in agreement with previous studies (e.g., Kiladis et al. 2006). Over the Atlantic region, this disturbance propagates at ~8.0 m s^{-1}. The circulation pattern associated with this disturbance closely resembles those previously documented over Africa (Kiladis et al. 2006). A statistically significant convectively coupled circulation is observed on day −1 over the west coast of Africa (Fig. 4d). The perturbation streamfunction on day −1 indicates that the TD signature over the Atlantic Ocean comes from preexisting easterly waves over Africa. At day 0 (Fig. 4e), the maximum convection has propagated westward, and the T_b signal depicts a southwest to northeast tilt with southerly and northerly flow in the region of enhanced and suppressed convection, respectively. Two days later (day +2; Fig. 4f), the convective anomalies move toward the extreme north of South America and the Caribbean region, becoming the potential precursors of TD activity over Central America and the eastern Pacific (Serra et al. 2010).

f. The MJO-W

Figures 5a–c show the regressed T_b and circulation fields at 850 hPa by using PC1 of Madden–Julian oscillation over the Western Hemisphere (MJO-W)–filtered T_b, which explains about 16.8% of the filtered variance (Table 1). The regressed fields exhibit a zonal wavenumber-1–2 structure that propagates eastward at a phase speed of ~8.5 m s^{-1} over the Western Hemisphere. The dynamical and convection fields are similar to features documented in previous studies (Matthews 2000; Kiladis et al. 2005; Adames and Wallace 2014). The circulation is coupled with enhanced convection in the eastern Pacific and western Amazon at day −5 (Fig. 5a) and slowly propagates eastward during the following days. At the same time, suppressed convection can be observed over the Indo-Pacific warm pool region (day −5 and day 0). The convection features of the MJO in the Eastern Hemisphere are evident even though the EOF was calculated only considering the Western Hemisphere domain. The circulation fields also show the characteristic cyclonic Rossby gyres flanking the enhanced convection, mainly on day 0 and day +5 (Figs. 5b,c). Anomalous westerlies extend through and to the west of the region of maximum convection in a similar way to the MJO circulation features documented by Kiladis et al. (2005) and Adames and Wallace (2014). The dipole-like convective structure between southern South America and the South Atlantic convergence zone (e.g., Nogués-Paegle and Mo 1997; Vera et al. 2018; Mayta et al. 2020), which is the most distinct feature of the intraseasonal South American precipitation, is also apparent on day 0 and day +5, albeit with a weak amplitude.

4. Governing thermodynamics

In this section, we applied the criteria documented in Mayta et al. (2022) used to characterize Rossby-like waves as

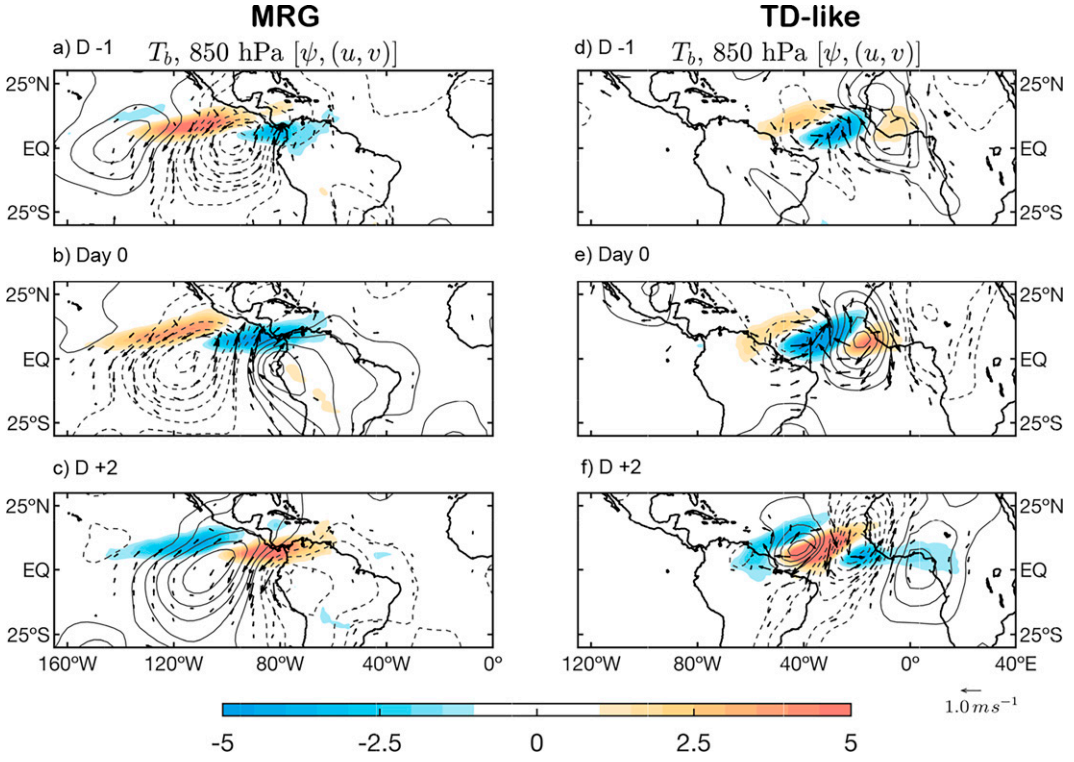

FIG. 4. As in Fig. 2, but for (left) MRG and (right) TD-like. Maps are for (top to bottom) day −1, day 0, and day +2. Contours are streamfunction, and the contour interval is 1.0×10^6 m^2 s^{-1}, with negative contours dashed.

a moisture mode but applied them to the remaining CCWs listed in Table 1. The three criteria proposed by the authors can be summarized as follows.

a. Moisture mode criterion 1 (C1): The wave must exhibit a large moisture signature that is highly correlated with the precipitation anomalies

For a disturbance to be considered a moisture mode, its signature in column water vapor ($\langle q' \rangle$) must be large enough to significantly modulate surface precipitation (P'). This results in a strong correlation (~0.9 rounded) between P' and $\langle q \rangle'$ because in the moisture modes column water vapor should explain the majority of the rainfall variance, defined as at least 80% in this study. Hereafter, $\langle \cdot \rangle \equiv 1/g \int_{100}^{1000} (\cdot) dp$, and primes ($'$) represent anomalies associated with each corresponding wave. In addition, we posit that the convective moisture adjustment time scale ($\tau_c = \langle q' \rangle / P'$) must be larger than 12 h (0.5 days) to guarantee a large moisture signature. Climatologically, τ_c varies from 6 to 24 h over the rainy regions of the tropics (Betts and Miller 1993; Bretherton et al. 2004; Dias and Pauluis 2010; Sobel and Maloney 2012; Jiang et al. 2016; Adames and Kim 2016).

We apply this criterion by constructing a scatterplot between P' and $\langle q' \rangle$ (Fig. 6a), where the slope of the linear fit gives the value of τ_c. The τ_c values and the correlation coefficient for all disturbances are summarized in Table 2. Results show that only the TD-like wave passes the first criterion, with correlations of ~0.9 and a τ_c value of 0.69 days. It is also clear that τ_c is smaller for WIG, EIG, Kelvin, and MRG waves with τ_c values of 0.21, 0.29, 0.22, and 0.29 days. These values broadly resemble previous findings (e.g., Yasunaga et al. 2019; Adames et al. 2019), where the dominance of moisture ($\tau_c \geq 0.5$) at low frequencies are found. As documented in Wolding et al. (2020), small values of τ_c usually mean some other process is causing rainfall, leading the τ_c to decrease. In addition, moisture modes are harder to exist if the convective adjustment is short [see Ahmed et al. (2021) for more details]. The MJO-W wave is the only exception. Despite the wave exhibiting τ_c larger than 0.5, the correlation between moisture and precipitation is the lowest of the examined balanced modes (0.59).

b. Moisture mode criterion 2 (C2): The mode must obey the WTG approximation

The weak temperature gradient (WTG) approximation in the column-integrated dry static energy (DSE) budget can be expressed as

$$\nabla \cdot \langle s\mathbf{v} \rangle' \simeq \langle Q_1 \rangle', \tag{1}$$

where $s = C_p T + \phi$, $\mathbf{v} = u\mathbf{i} + v\mathbf{j}$ is the horizontal vector wind field, and Q_1 is the apparent heating rate. The column-integrated heating can be expressed in terms of ERA5 fields as

$$\langle Q_1 \rangle' \simeq \langle Q_r \rangle' + L_v P' + \mathrm{SH}', \tag{2}$$

where Q_r is the column radiative heating rate, SH is the surface sensible heat flux, and L_v is the latent heat of vaporization (2.5×10^6 J kg^{-1}).

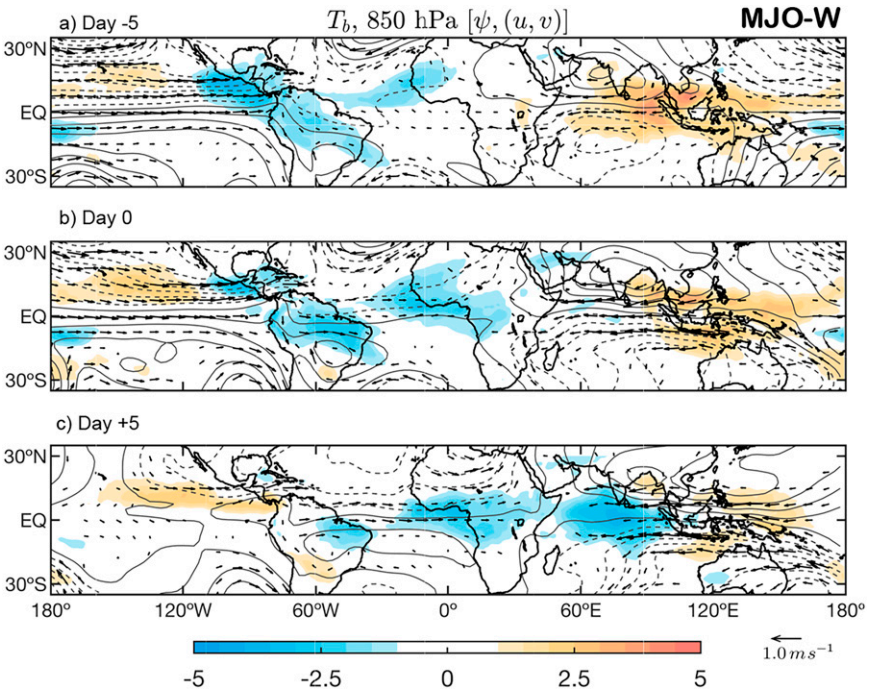

FIG. 5. As in Fig. 2, but for the MJO-W wave for (a) day −5, (b) day 0, and (c) day +5. Contours are streamfunction, and the contour interval is 2.0×10^6 m^2 s^{-1}, with negative contours dashed.

To pass this criterion, a wave must exhibit a high correlation (~0.9 rounded), and the slope must be within the margin of 0.9–1.1. In other words, a slope close to ~1 is needed to guarantee the WTG balance in Eq. (1). From Fig. 6b and Table 2, we can see that the correlation between column DSE divergence and Q_1 is near unity in all the wave types examined. However, the slope of the linear least squares fit of the two fields is smaller than ~0.9 in all except the MRG and TD-like waves. Thus, only these two wave types satisfy the WTG criterion.

c. *Moisture mode criterion 3 (C3): Moisture must govern the evolution of MSE*

Moisture modes occur when moisture is the main term contributor to MSE. This balance simply states that column water vapor approximately balances column MSE:

$$\langle m \rangle' \approx L_v \langle q \rangle', \tag{3}$$

where $m = s + L_v q$. The same conditions for the previous criterion are used to assess this one.

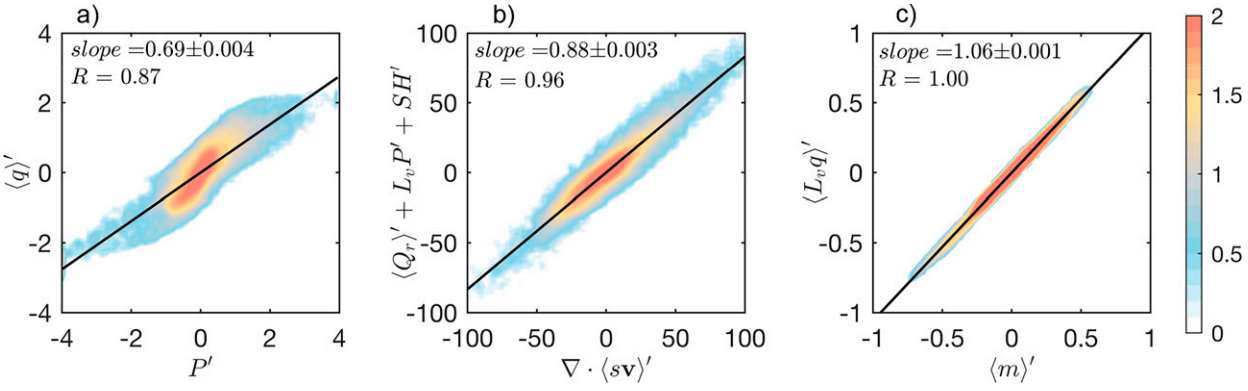

FIG. 6. Scatterplots of (a) P' vs $\langle q \rangle'$, (b) $\nabla \cdot \langle s\mathbf{v} \rangle'$ vs $\langle Q_r \rangle' + L_v P' + \mathrm{SH}'$, and (c) $\langle m \rangle'$ vs $\langle L_v q \rangle'$ for the TD-like waves. The shading represents the base-10 logarithm of the number of points within 0.1 mm × 0.1 mm bins in (a), 2 W m^{-2} × 2 W m^{-2} bins in (b), and 2.5×10^5 J m^{-2} × 2.5×10^5 J m^{-2} bins in (c). Anomalies are obtained by regressing all fields against the PC1 (normalized, TD-like) over the 0°–15°N, 60°–0°W domain. The linear fit obtained from linear least squares fit is shown as a solid black line. The slope of the linear fit and the correlation coefficient are shown in the top-left of each panel.

TABLE 2. Moisture mode criteria applied to each type of CCWs. The slope of the linear fit and the correlation coefficient (Corr) are shown in a similar manner to Fig. 6. The values for the Rossby-like mode come from Mayta et al. (2022).

	C1: $P' \propto \langle q \rangle'$			C2: $\nabla \cdot \langle s\mathbf{v} \rangle' \simeq \langle Q_1 \rangle'$			C3: $\langle m \rangle' \approx L_v \langle q \rangle'$		
	Slope	Corr	Result	Slope	Corr	Result	Slope	Corr	Result
WIG	0.21 ± 0.005	0.86	×	0.56 ± 0.009	0.94	×	1.16 ± 0.021	0.92	×
EIG	0.29 ± 0.004	0.81	×	0.66 ± 0.005	0.93	×	1.15 ± 0.006	0.97	×
Kelvin	0.22 ± 0.003	0.79	×	0.80 ± 0.002	0.99	×	0.71 ± 0.009	0.78	×
MRG	0.29 ± 0.003	0.77	×	0.85 ± 0.004	0.96	✓	1.09 ± 0.003	0.98	✓
TD-like	0.69 ± 0.004	0.87	✓	0.88 ± 0.003	0.96	✓	1.06 ± 0.001	1.00	✓
MJO-W	0.61 ± 0.003	0.59	×	0.83 ± 0.001	0.95	×	0.68 ± 0.001	0.92	×
Rossby-like	1.63 ± 0.007	0.96	✓	0.99 ± 0.002	0.99	✓	1.04 ± 0.002	0.99	✓

From Fig. 6c, we see that the slope of the linear fit is ~1 for the TD-like wave. The other disturbance that satisfies this criterion is MRG waves, with a slope value of 1.09 (Table 2).

When all conditions are examined together, we see that only the TD-like and Rossby-like waves pass the three criteria and hence can be considered to be moisture modes.

d. N_{mode}

In addition to the three aforementioned criteria, we can also estimate the value of N_{mode} to classify the existing tropical waves. N_{mode} is a nondimensional scale that measures the relative amplitude of C_pT to L_vq; N_{mode} can be computed as in Adames et al. (2019):

$$N_{\text{mode}} \simeq \frac{c_p^2 \tau}{c^2 \tau_c}, \tag{4}$$

where c is the phase speed of a first baroclinic free gravity wave ($c \simeq 50$ m s^{-1}), c_p is phase speed of the wave, τ_c is the convective moisture adjustment time scale, and $\tau = \lambda/c_p$ is the temporal time scale with λ being the wavelength. When $N_{\text{mode}} \ll 1$, moisture governs the thermodynamics of a wave, resulting in moisture modes, but if $N_{\text{mode}} \gg 1$, the thermodynamics of a wave are predominantly driven by thermal fluctuations, resulting in gravity wave. When $N_{\text{mode}} \approx 1$ the wave will exhibit behavior of both the moisture mode and gravity wave. Table 3 shows the values of the parameters in Eq. (4) along with the obtained value of N_{mode}. The largest value of N_{mode} is seen in EIG waves, with a value of about 5. The EIG wave is the only wave type in which N_{mode} is substantially larger than unity and hence temperature fluctuations are more important than moisture fluctuations in their thermodynamics, as in pure gravity waves. On the other hand, WIG, MRG, and the Kelvin waves have N_{mode} values near unity, suggesting that moisture and temperature play comparable roles in their thermodynamics. With an N_{mode} value of 1.36, the MJO-W value is also sufficiently close to unity and may also be considered a mixed system. Only TD-like waves have N_{mode} values that are much smaller than unity ($N_{\text{mode}} = 0.18$). This is also the only wave that passes the three moisture mode criteria outlined above.

TABLE 3. N_{mode} values for CCWs. The phase speed (c_p) is calculated by using the Radon transform method [more details in Mayta and Adames (2021)]. The convective moisture adjustment time scale (τ_c) is estimated as the slope of the linear fit in the scatterplot of Fig. 6. The values for the Rossby-like mode come from Mayta et al. (2022).

	c_p (m s^{-1})	τ (days)	τ_c (days)	N_{mode}
WIG	25.6	2.1	0.21	2.62
EIG	32.5	3.4	0.29	4.95
Kelvin	15.8	6.25	0.22	2.84
MRG	19.5	4.8	0.29	2.52
TD-like	8.0	5.1	0.69	0.18
MJO-W	8.5	28.75	0.61	1.36
Rossby-like	5.4	13.7	1.63	0.10

5. MSE budget

a. MSE budget analysis in reanalysis

The column-integrated MSE budget is defined as in Yanai et al. (1973):

$$\frac{\partial \langle m \rangle'}{\partial t} = -\langle \mathbf{v} \cdot \nabla m \rangle' - \left\langle \omega \frac{\partial m}{\partial p} \right\rangle' + \langle Q_r \rangle' + \underbrace{L_v E' + \text{SH}'}_{S_f'}, \tag{5}$$

where $m \equiv s + L_vq$ is MSE. The left-side term in Eq. (5) is the MSE tendency. The first and second terms on the right side of the equation represent horizontal MSE advection and vertical MSE advection, respectively. The other terms in Eq. (5) are MSE source terms: the radiative heating rate, surface latent heat flux L_vE, and surface sensible heat flux. In this study, L_vE' and SH′ are analyzed together as surface fluxes S_f'. In addition, following previous studies (e.g., Andersen and Kuang 2012; Adames 2017; among others), we estimate the contribution of different processes to the propagation and maintenance of the CCWs by projecting each MSE budget term upon the MSE tendency and the MSE anomalies, respectively, i.e.,

$$\text{Proj}(F, \partial\langle m \rangle/\partial t) = \frac{\|F \times \partial\langle m \rangle/\partial t\|}{\|\partial\langle m \rangle/\partial t \times \partial\langle m \rangle/\partial t\|}, \tag{6a}$$

$$\text{Proj}(F, \langle m \rangle) = \frac{\|F \times \langle m \rangle\|}{\|\langle m \rangle \times \langle m \rangle\|}, \tag{6b}$$

where F is each individual term in Eq. (5). The term $\|\cdot\|$ implies an areal average from the corresponding lag regressions

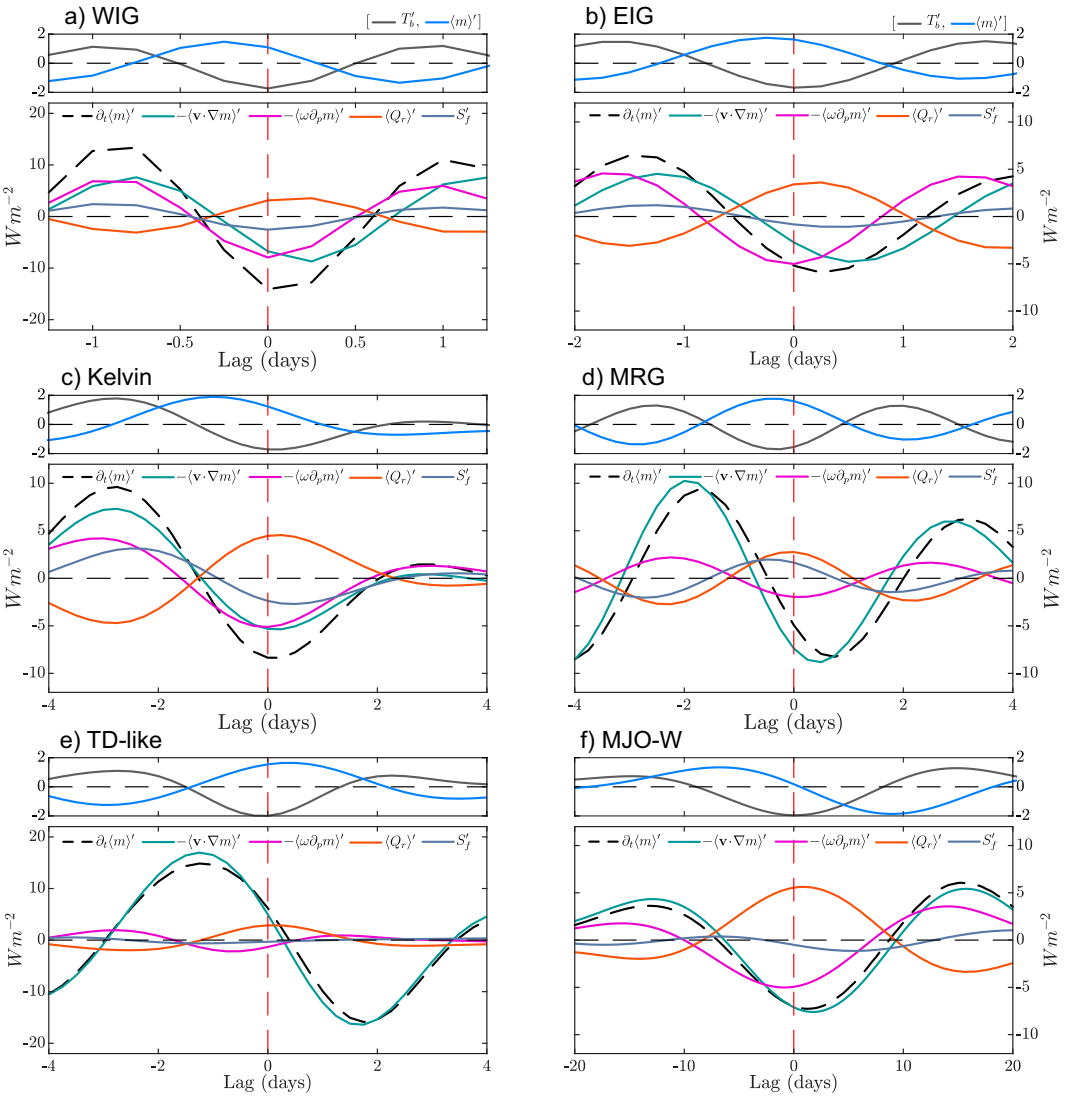

FIG. 7. The larger bottom plot for each panel shows the area-average anomaly terms of the column MSE budget of Eq. (5): $\partial_t\langle m\rangle'$ (dashed black), $-\langle \mathbf{v}\cdot\nabla m\rangle'$ (green), $-\langle \omega\partial_p m\rangle'$ (magenta), $\langle Q_r\rangle'$ (dark orange), and S_f' (light blue). The smaller top plot for each panel shows the evolution of the T_b (gray) and column MSE (light blue). Lag regression of budget terms are based on PC1 time series (normalized) of the corresponding CCWs averaged over 10°S–10°N, 80°–20°W for WIG, EIG, Kelvin, and MJO-W waves; 0°–15°N, 120°–70°W for MRGs; and 0°–15°N, 60°–0°W for TD-like wave. Anomalies are scaled to one standard deviation PC perturbation of the corresponding CCWs.

described in Fig. 7. The lags used for the calculation represent a cycle of the corresponding wave. The areas considered are 10°S–10°N, 80°–20°W for WIG, EIG, Kelvin, and MJO-W waves; 0°–15°N, 120°–70°W for MRGs; and 0°–15°N, 60°W–0° for TD-like waves. The chosen area represents the region where the wave is most active.

Figure 7 shows the composite time series of each budget term in Eq. (5) for the different CCWs. Column-integrated MSE $\langle m\rangle'$ leads convection in fast-propagating waves (WIG, EIG, and Kelvin), with the fields being nearly in quadrature. The $\langle m\rangle'$ peaking before convection was also documented during TOGA COARE for high-frequency disturbances (Inoue and Back 2015). The $\langle m\rangle'$ anomalies and convection are also evolving in quadrature for the slow-propagating MJO-W wave (Fig. 7f). For balanced MRG, convection is almost in phase with $\langle m\rangle'$ (Fig. 7d). A TD-like wave is an exception because $\langle m\rangle'$ peaks just after the wave (Fig. 7e).

The horizontal advection $-\langle \mathbf{v}\cdot\nabla m\rangle'$ exhibits different behaviors among the different CCWs. The amplitude of the variations in $-\langle \mathbf{v}\cdot\nabla m\rangle'$ becomes greater as the wave propagates more slowly. Indeed, $-\langle \mathbf{v}\cdot\nabla m\rangle'$ agrees with the tendency of column-integrated MSE($\partial_t\langle m\rangle'$ in MRG, TD-like, and MJO-W waves (Figs. 8d–f). It means that on these waves most of the recharge–discharge cycle of MSE is explained by the $-\langle \mathbf{v}\cdot\nabla m\rangle'$, while the other terms cancel each other out. For fast-propagating divergent waves (WIG, EIG, and Kelvin), the magnitude of

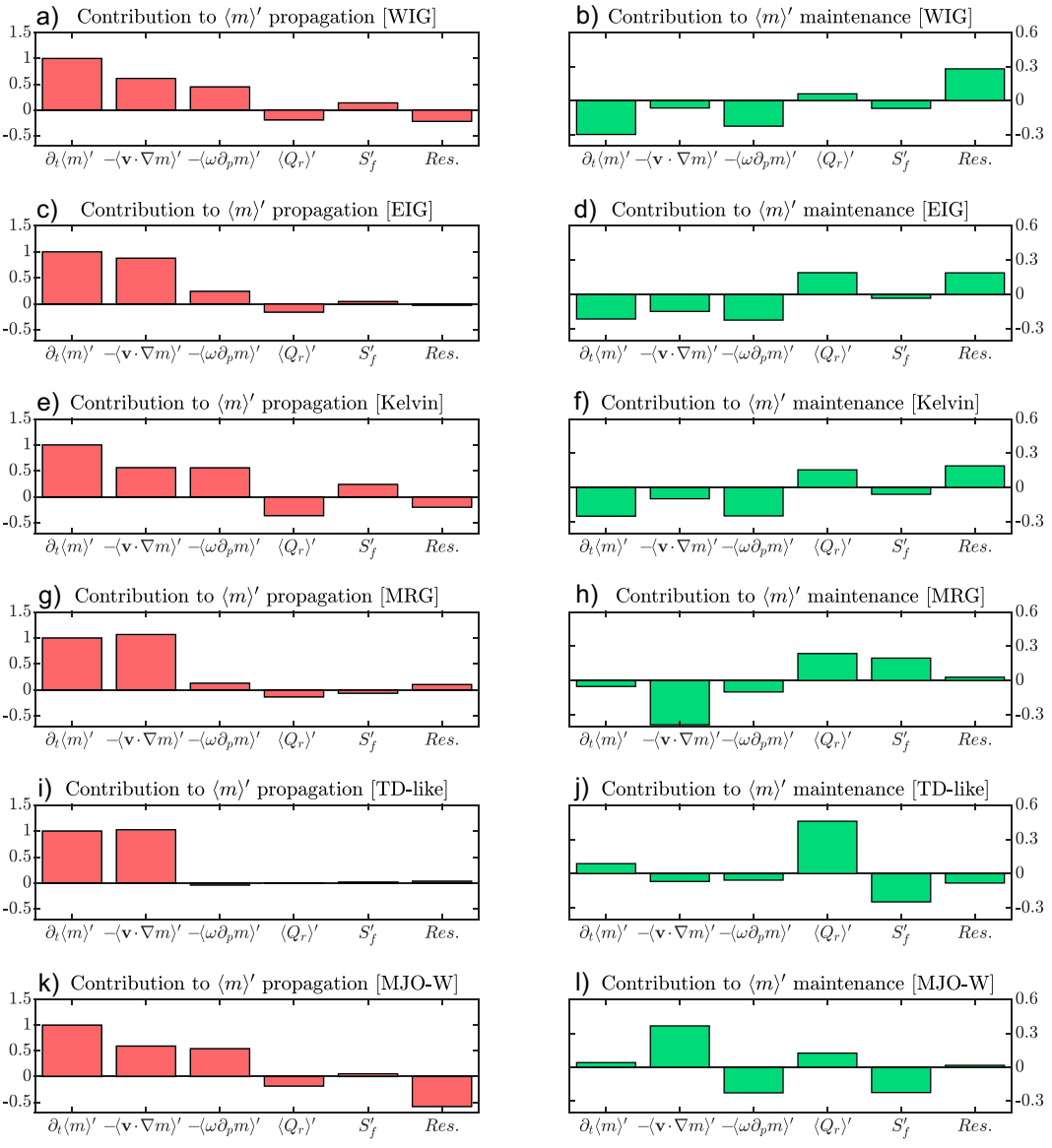

FIG. 8. Normalized contribution of the column-integrated right-hand-side terms in Eq. (5) to the (left) propagation and (right) maintenance of the CCWs. Area-averaged weighted projections are over 10°S–10°N, 80°–20°W for WIG, EIG, Kelvin, and MJO-W waves; 0°–15°N, 120°–70°W for MRGs; and 0°–15°N, 60°W –0° for TD-like waves.

$-\langle \mathbf{v} \cdot \nabla m \rangle'$ is smaller or comparable to the vertical advection. Analyzing the relative contribution to the propagation, we see that $-\langle \mathbf{v} \cdot \nabla m \rangle'$ is the largest contributor to the propagation of the MSE in the CCWs, except in Kelvin (Fig. 8e). For the MJO-W, $-\langle \mathbf{v} \cdot \nabla m \rangle'$ also plays the main role in its maintenance (Fig. 8l).

The column-integrated vertical MSE advection $-\langle \omega \partial_p m \rangle'$ also differs among the different CCWs. While the $-\langle \mathbf{v} \cdot \nabla m \rangle'$ is the dominant term in rotational modes (MRG and TD-like), the $-\langle \omega \partial_p m \rangle'$ term is comparable to or even larger than $-\langle \mathbf{v} \cdot \nabla m \rangle'$ in the divergent waves (WIG, EIG, and Kelvin; Figs. 7a–c). Analyzing the relative importance of the terms in Eq. (5) to the propagation of MSE shows that $-\langle \omega \partial_p m \rangle'$ plays a key role in the propagation of Kelvin waves (Fig. 8e). In the MJO-W, the $-\langle \omega \partial_p m \rangle'$ plays a similar role to that of $-\langle \mathbf{v} \cdot \nabla m \rangle'$ (Fig. 8k).

Column-integrated radiative heating $\langle Q_r \rangle'$ is approximately in phase with the convection (or the convection leads slightly) on all the CCWs. It is nearly in phase with the MSE in the TD-like wave, where it is the largest contributor to its maintenance (Fig. 8j) but substantially lags it for the other waves. $\langle Q_r \rangle'$ also plays an important role in the maintenance of MRG, but it does not play a significant role in the maintenance of MSE in the remaining CCWs.

Finally, surface fluxes S_f' vary almost out–off phase with $\langle Q_r \rangle'$ and convection itself on all the CCWs, except on MRG

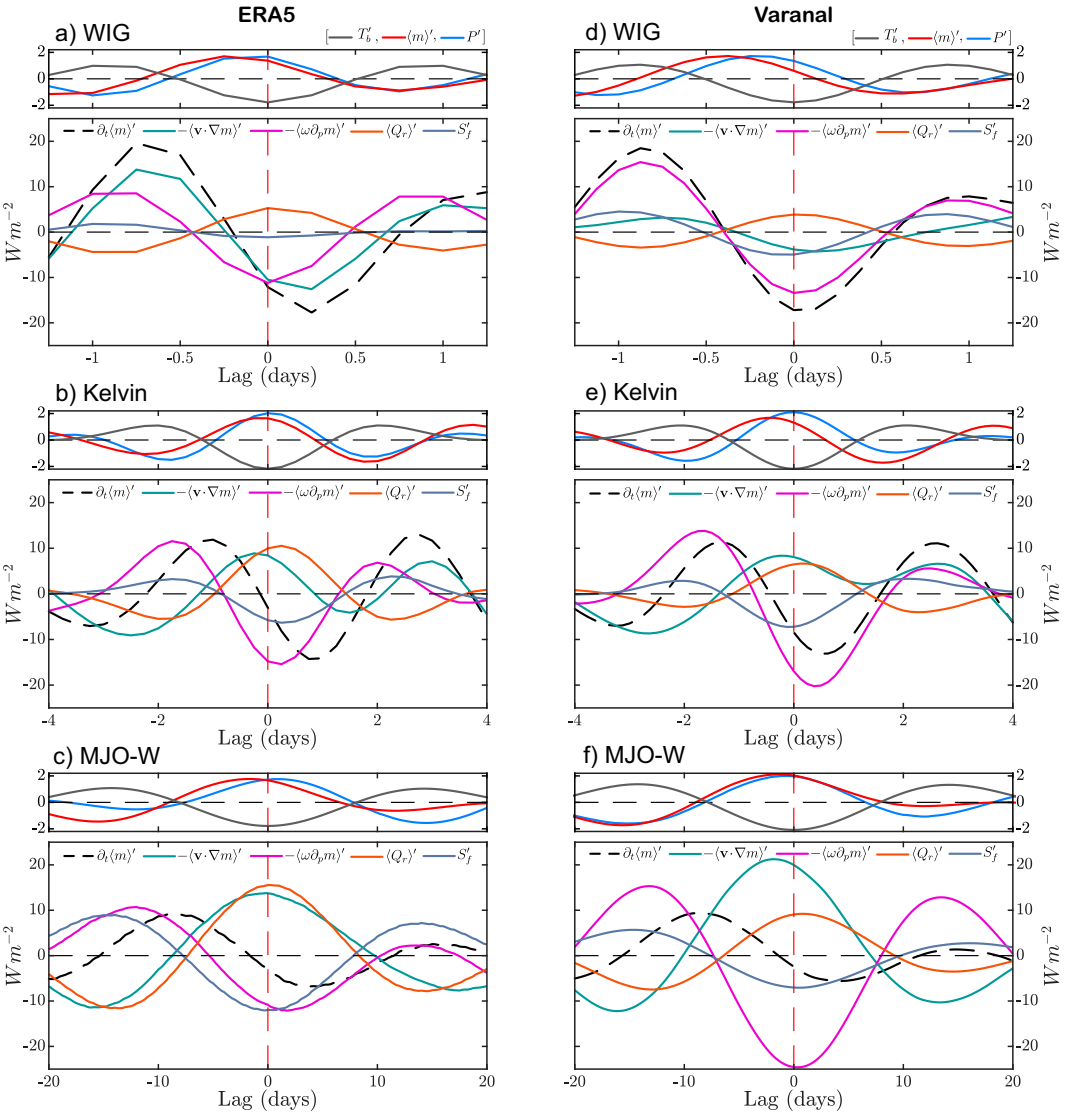

FIG. 9. As in Fig. 7, but the lag regression is calculated based on (top) WIG, (middle) Kelvin, and (bottom) MJO-W filtered T_b' time series at the GoAmazon base point (3.15°S, 60.6°W). The budget terms evolution from (left) ERA5 and (right) VARANAL. The top plot in each panel shows the evolution of the standardized T_b' (gray), $\langle m\rangle'$ (red), and precipitation (blue). Anomalies are scaled to −4.5 K perturbation in WIG wave, −8.5 K in Kelvin wave, and −5.0 K MJO-W wave T_b' at lag 0 and the GoAmazon base point.

waves. Inoue and Back (2015) also showed similar variations of the surface fluxes and radiative terms with respect to the MSE tendency in TOGA COARE. Surface fluxes are only important for MRG wave maintenance (Fig. 8h). In the remaining waves, its contribution to either propagation or maintenance is either negligible or contributes to decay (TD-like and MJO-W).

b. *MSE budget analysis during GoAmazon 2014/15 field campaign: A focus on the skill of ERA5*

It is well known that analysis increments and misrepresentation of subgrid-scale processes largely contribute to the residual observed in the MSE budget in reanalysis data, as documented recently in Ren et al. (2021). Indeed, significant budget residuals are seen for most of the CCWs examined here (Fig. 8). In this section, we compare the MSE budget results of reanalysis to those from the "observation-based" MSE budget data collected during the GoAmazon 2014/15 field campaign. The analyses are focused only on three disturbances: WIG, Kelvin, and MJO-W waves because these are the only waves that exhibit a significant amount of variance over the GoAmazon site (Fig. 1). For the ERA5 data, we used the same grid point of the GoAmazon field campaign (3.15°S, 60.6°W) and the same 2014/15 period (Figs. 9, 10).

The results from GoAmazon 2014/15 qualitatively agree with those from reanalysis, although important differences

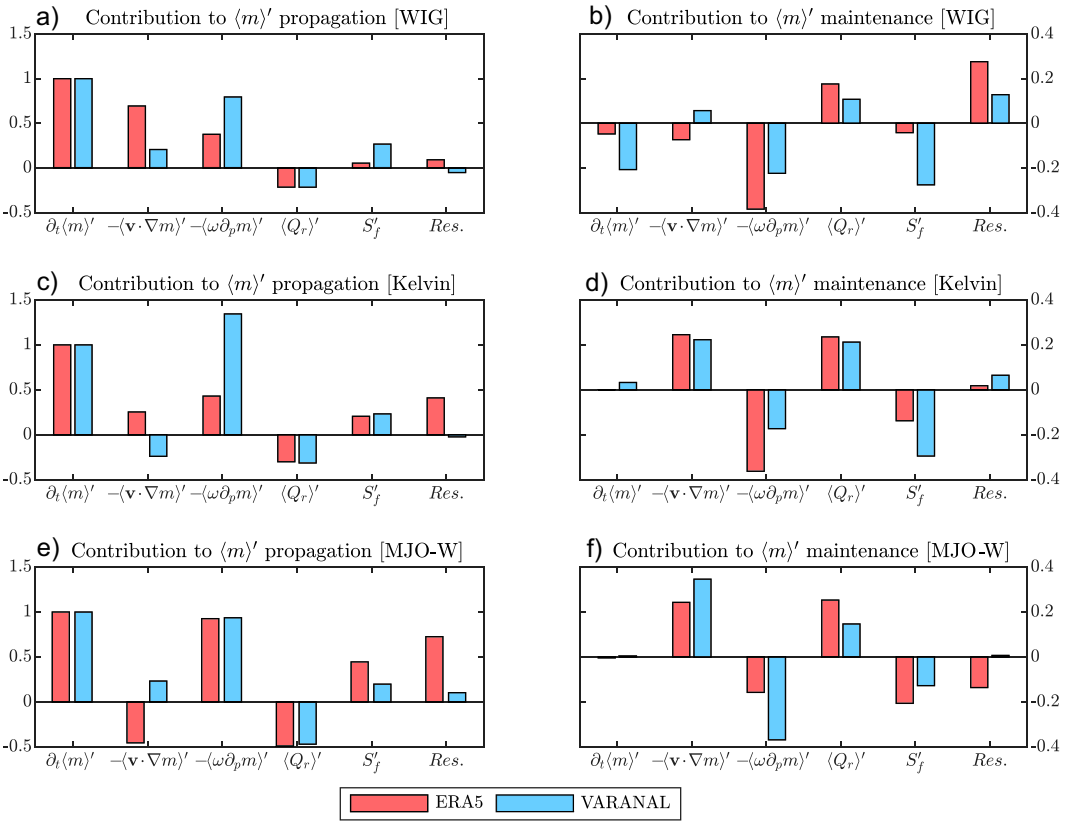

FIG. 10. As in Fig. 8, but using ERA5 (red bars) and VARANAL GoAmazon data (blue bars) at the base point 3.15°S, 60.6°W.

are observed in the budget terms. For WIG and Kelvin waves, $\langle m\rangle'$ slightly leads T_b' and precipitation in both datasets (top panels in Figs. 9a–e). In MJO-W, $\langle m\rangle'$ leads precipitation in reanalysis (Fig. 9c), but in VARANAL $\langle m\rangle'$ and precipitation evolve almost in-phase (Fig. 9f). This suggests that $\langle m\rangle'$ is tightly connected to convection and precipitation itself and can be used to understand the evolution of the precipitation anomaly associated with each wave.

The advective terms also exhibit differences between ERA5 and VARANAL. In WIGs, $-\langle \mathbf{v}\cdot\boldsymbol{\nabla} m\rangle'$ is approximately in phase with and of a similar magnitude as the tendency of column-integrated MSE ($\partial_t\langle m\rangle'$) in ERA5. However, the evolution of $-\langle \mathbf{v}\cdot\boldsymbol{\nabla} m\rangle'$ in VARANAL is roughly 3 times smaller than in ERA5 (Fig. 9b). The results from VARANAL are more consistent with the WIG waves documented in the TOGA COARE data than those from the collocated ERA5 data [see Fig. 2 in Inoue and Back (2015)]. For Kelvin and MJO-W waves, $-\langle \mathbf{v}\cdot\boldsymbol{\nabla} m\rangle'$ shows similar evolution and magnitude.

The behavior of $-\langle\omega\partial_p m\rangle'$ also differs in both datasets. For the WIG and Kelvin waves, even though $-\langle\omega\partial_p m\rangle'$ is similar in magnitude in ERA5 and VARANAL, $-\langle\omega\partial_p m\rangle'$ evolves in phase with the $\partial_t\langle m\rangle'$ in VARANAL and the other terms tend to cancel one another. In contrast, $-\langle\omega\partial_p m\rangle'$ and $\partial_t\langle m\rangle'$ are almost in quadrature in ERA5. Last, the $-\langle\omega\partial_p m\rangle'$ in MJO-W is about twice as large as that in ERA5, although they are roughly in phase (Fig. 9f).

Finally, the $\langle Q_r\rangle'$ and S_f' in both datasets show almost the same magnitude and phase evolution in WIG, Kelvin, and MJO-W waves. An exception occurs for the WIG waves, where S_f' shows a larger amplitude in VARANAL during convective evolution (Fig. 9d), while a negligible contribution in ERA5 is observed.

The differences observed between ERA5 and VARANAL in Fig. 9 can be further investigated by projecting each budget term by using Eqs. (6a) and (6b). The bar plots in Fig. 10 show a smaller budget residual in VARANAL data. The WIG wave is an exception, where a nonnegligible residual is still observed in its maintenance (Fig. 10b). The residual seen here may be a result of numerical errors or due to the fact that the MSE budget is not exact (e.g., Neelin 2007; Randall 2015). The second difference between ERA5 and VARANAL is observed in the advective terms. While the $-\langle \mathbf{v}\cdot\boldsymbol{\nabla} m\rangle'$ primarily propagates the WIG wave in ERA5, $-\langle\omega\partial_p m\rangle'$ plays the main role in the westward propagation of the wave in VARANAL (Fig. 10a). Even though Kelvin waves propagate eastward due to $-\langle\omega\partial_p m\rangle'$ in both datasets (Fig. 10c), its contribution to propagation is much larger in VARANAL. The MJO-W propagates eastward due to $-\langle\omega\partial_p m\rangle'$ in both datasets, and the contributions are similar (Fig. 10e). Overall, the contribution from $-\langle \mathbf{v}\cdot\boldsymbol{\nabla} m\rangle'$ is overestimated in reanalysis, while the contribution from $-\langle\omega\partial_p m\rangle'$ is underestimated.

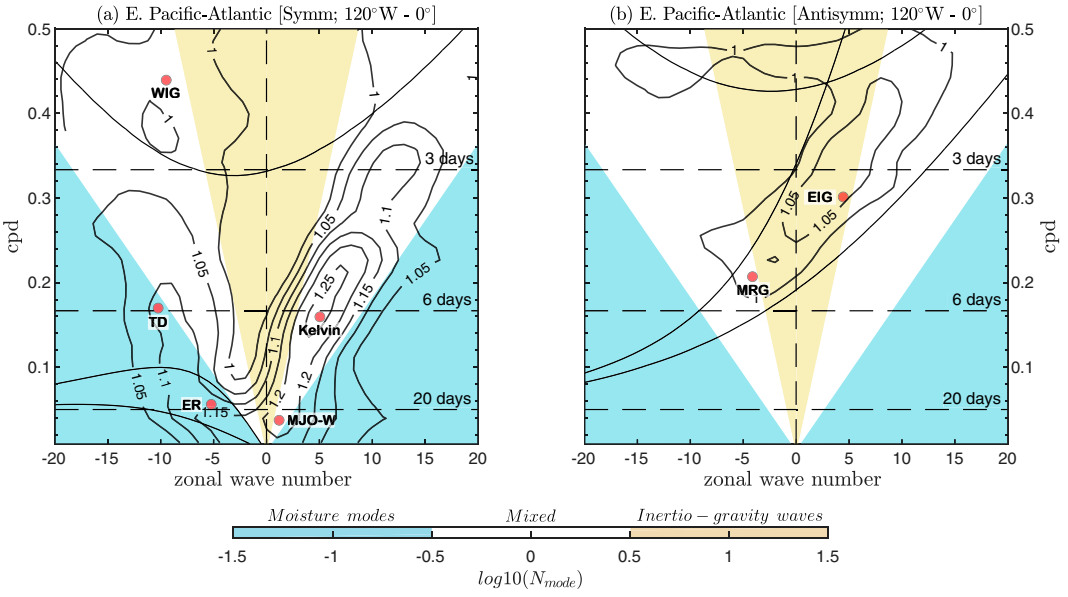

FIG. 11. Regional wavenumber–frequency power spectrum (contours) of the (a) symmetric and (b) antisymmetric component of CLAUS T_b calculated for 10°N–10°S, 120°W–0°. The solid dispersion curves correspond to 8- and 70-m equivalent depths. The functional form of the tapering window is the same as described in Wheeler and Kiladis (1999). Background spectra were estimated separately for the regional domain, using the smoothing procedure of Dias and Kiladis (2014). Contour interval is 0.05. Shadings represent wavenumber–frequency distribution of base 10 logarithm of N_{mode} following a similar procedure of Adames (2022). Blue shading represents tropical systems that can be categorized as moisture modes, yellow shading can be considered inertio-gravity waves, and white represents mixed systems. Orange circles approximately represent the average zonal wavenumber and frequency of each CCWs.

6. Summary and conclusions

In this study, we sought to characterize the thermodynamic processes of convectively coupled waves (CCWs) over the Western Hemisphere. EOF analysis was applied to filtered satellite brightness temperature T_b over the Western Hemisphere (10°S–15°N, 120°W–0°), considering the region of maximum variance of each CCW (Fig. 1). The composite dynamical structures and convection of CCWs depict an evolution that agrees with previous observational studies of tropical waves over other locations (e.g., Takayabu 1994; Wheeler and Kiladis 1999; Wheeler et al. 2000; Straub and Kiladis 2002; Kiladis et al. 2005; Yang et al. 2007; Kiladis et al. 2009, 2016; Mayta et al. 2021).

By using the three criteria to identify moisture modes, we demonstrated that the TD-like wave may be considered a moisture mode (Fig. 6 and Table 2), similar to the Rossby-like wave documented recently in Mayta et al. (2022). These waves also exhibit an N_{mode} parameter (Adames et al. 2019; Adames 2022) that is much smaller than unity, another requirement necessary to categorize a wave as a moisture mode. Our results indicate that slowly evolving rotational tropical waves are likely to be moisture modes, as Adames (2022) posited. These features can also be clearly discerned from Fig. 11a where Rossby-like and a large portion of the TD-like waves spectrum fall into the moisture mode category. These results are consistent with Inoue et al. (2020), who also indicated that equatorial Rossby waves and TD-like waves have characteristics of moisture modes (see their Fig. 7).

We also found that EIG waves are the only CCW in the Western Hemisphere whose thermodynamics are dominated by temperature fluctuations. It exhibits the fastest phase speed at 32.5 m s^{-1} and an N_{mode} value of ~5.0 (Table 3). It is the only wave that falls into the gravity wave end of the spectrum shown in Fig. 11b.

None of the remaining waves, the Kelvin, WIG, MRG, and MJO-W, satisfy the three criteria necessary to be categorized as moisture modes and exhibit N_{mode} values that are close to unity (ranging from 1.36 to 2.84). Thus, most of the CCWs explored over the Western Hemisphere are mixed systems in which temperature and moisture play comparable roles in their thermodynamics (see white dispersion in Fig. 11). It is particularly noteworthy that the MJO-W wave does not satisfy the criteria to be considered a moisture mode. As shown in Fig. 11a, the power spectrum is centered in wavenumbers ~1–2 and falls within the region of the spectrum where N_{mode} is near unity, supporting our finding that the MJO-W is a mixed system with intermediate properties of moisture mode and gravity and/or Rossby waves (Adames and Maloney 2021; Adames 2022). These results are in agreement with Powell (2017), who suggested that MJO variability exhibits moisture mode behavior only over the Indo-Pacific warm pool region. More work is currently being done to assess the characteristics of the MJO throughout the globe.

The processes that govern MSE evolution also differ among CCWs. The column-integrated vertical MSE advection $-\langle\omega\partial_p m\rangle'$ was identified as the primarily contributor to the MSE propagation

in most of all divergent wave types (WIG, Kelvin; Figs. 7, 9) as well as the MJO-W wave. The horizontal MSE advection $-\langle \mathbf{v} \cdot \nabla m \rangle'$, on the other hand, is the most important budget term contributor to the propagation in rotational disturbance types such as MRG and TD-like waves.

We compared the results from ERA5 with observational data from the VARANAL GoAmazon 2014/15 field campaign. Analyses of the MSE budget terms of the WIGs, Kelvin, and the MJO-W waves revealed differences between ERA5 and VARANAL data. In all three CCWs examined, the role of vertical MSE advection in MSE propagation is significantly underestimated. This difference is especially notable in WIG and Kelvin evolution where the VARANAL and ERA5 data disagree on whether horizontal or vertical MSE advection drives MSE propagation. Based on these results, we can conclude that ERA5 severely underestimates the role of vertical MSE advection in CCWs in the Western Hemisphere. This result may partially explain the budget residuals we found in ERA5 data.

In conclusion, our results show a diversity in CCWs in the Western Hemisphere. We see evidence for both equatorial and off-equatorial moisture modes, as recently suggested in Adames (2022). We also found evidence for mixed systems where temperature and moisture play the same role. Results also suggest that the MJO over the Western Hemisphere behaves like a Kelvin wave, both having intermediate properties between the gravity wave and moisture mode. We also found major disagreements between reanalysis and observation-based datasets, suggesting major deficiencies in reanalysis. This may be due to limitations in convection representation but also from a lack of in situ observations in the region (Diniz et al. 2020). Future work should seek to address a large residual observed in the MSE budget in the reanalysis dataset. It should include the evaluation of the accuracy of applying MSE budgets to understand the thermodynamics of tropical motions.

Acknowledgments. VM and ÁFA were supported by NSF CAREER Grant 2236433 and by the University of Wisconsin startup package. VM and ÁFAC were also supported by NOAA Grant NA22OAR4310611. VM would like to thank Chelsea Snide for discussions that helped improve this manuscript. We also would like to thank George Kiladis for providing us the CLAUS satellite data used in this study.

Data availability statement. ERA5 data are available at https://www.ecmwf.int/en/forecasts/datasets/reanalysis-datasets/era5/). The VARANAL product is available to the community at the Atmospheric Radiation Measurement program archive at https://iop.archive.arm.gov/arm-iop/0eval-data/xie/scm-forcing/iop_at_mao/GOAMAZON/2014-2015/. Interpolated T_b data are provided by the NOAA/ESRL.

REFERENCES

Adames, Á. F., 2017: Precipitation budget of the Madden–Julian oscillation. *J. Atmos. Sci.*, **74**, 1799–1817, https://doi.org/10.1175/JAS-D-16-0242.1.

——, 2022: The basic equations under weak temperature gradient balance: Formulation, scaling, and types of convectively coupled motions. *J. Atmos. Sci.*, **74**, 2087–2108, https://doi.org/10.1175/JAS-D-21-0215.1.

——, and J. M. Wallace, 2014: Three-dimensional structure and evolution of the MJO and its relation to the mean flow. *J. Atmos. Sci.*, **71**, 2007–2026, https://doi.org/10.1175/JAS-D-13-0254.1.

——, and D. Kim, 2016: The MJO as a dispersive, convectively coupled moisture wave: Theory and observations. *J. Atmos. Sci.*, **73**, 913–941, https://doi.org/10.1175/JAS-D-15-0170.1.

——, and E. D. Maloney, 2021: Moisture mode theory's contribution to advances in our understanding of the Madden-Julian oscillation and other tropical disturbances. *Curr. Climate Change Rep.*, **7**, 72–85, https://doi.org/10.1007/s40641-021-00172-4.

——, D. Kim, S. K. Clark, Y. Ming, and K. Inoue, 2019: Scale analysis of moist thermodynamics in a simple model and the relationship between moisture modes and gravity waves. *J. Atmos. Sci.*, **76**, 3863–3881, https://doi.org/10.1175/JAS-D-19-0121.1.

——, S. W. Powell, F. Ahmed, V. C. Mayta, and J. D. Neelin, 2021: Tropical precipitation evolution in a buoyancy-budget framework. *J. Atmos. Sci.*, **78**, 509–528, https://doi.org/10.1175/JAS-D-20-0074.1.

Ahmed, F., J. D. Neelin, and Á. F. Adames, 2021: Quasi-equilibrium and weak temperature gradient balances in an equatorial beta-plane model. *J. Atmos. Sci.*, **78**, 209–227, https://doi.org/10.1175/JAS-D-20-0184.1.

Andersen, J. A., and Z. Kuang, 2012: Moist static energy budget of MJO-like disturbances in the atmosphere of a zonally symmetric aquaplanet. *J. Climate*, **25**, 2782–2804, https://doi.org/10.1175/JCLI-D-11-00168.1.

Betts, A. K., and M. J. Miller, 1993: The Betts-Miller scheme. *The Representation of Cumulus Convection in Numerical Models*, *Meteor. Monogr.*, No. 46, Amer. Meteor. Soc., 107–121, https://doi.org/10.1007/978-1-935704-13-3_9.

Bretherton, C. S., M. E. Peters, and L. E. Back, 2004: Relationships between water vapor path and precipitation over the tropical oceans. *J. Climate*, **17**, 1517–1528, https://doi.org/10.1175/1520-0442(2004)017%3C1517:RBWVPA%3E2.0.CO;2.

Dias, J., and O. Pauluis, 2010: Impacts of convective life-time on moist geostrophic adjustment. *J. Atmos. Sci.*, **67**, 2960–2971, https://doi.org/10.1175/2010JAS3405.1.

——, and G. N. Kiladis, 2014: Influence of the basic state zonal flow on convectively coupled equatorial waves. *Geophys. Res. Lett.*, **41**, 6904–6913, https://doi.org/10.1002/2014GL061476.

Diniz, F. L. R., R. Todling, and D. L. Herdies, 2020: A brief assessment of the impact of nearly 40 years of assimilated observations over the amazon basin. *Earth Space Sci.*, **7**, e2019EA000779, https://doi.org/10.1029/2019EA000779.

Gonzalez, A. O., and X. Jiang, 2019: Distinct propagation characteristics of intraseasonal variability over the tropical West Pacific. *J. Geophys. Res. Atmos.*, **124**, 5332–5351, https://doi.org/10.1029/2018JD029884.

Haertel, P. T., and G. N. Kiladis, 2004: Dynamics of 2-day equatorial waves. *J. Atmos. Sci.*, **61**, 2707–2721, https://doi.org/10.1175/JAS3352.1.

Hannah, W. M., and E. D. Maloney, 2014: The moist static energy budget in NCAR CAM5 hindcasts during DYNAMO. *J. Adv. Model. Earth Syst.*, **6**, 420–440, https://doi.org/10.1002/2013MS000272.

Hersbach, H., and Coauthors, 2019: Global reanalysis: Goodbye ERA-interim, hello ERA5. *ECMWF Newsletter*, No. 159, ECMWF, Reading, United Kingdom, 17–24, https://doi.org/10.21957/vf291hehd7.

Hodges, K. I., D. W. Chappell, G. J. Robinson, and G. Yang, 2000: An improved algorithm for generating global window brightness temperatures from multiple satellite infrared imagery. *J. Atmos. Oceanic Technol.*, **17**, 1296–1312, https://doi.org/10.1175/1520-0426(2000)017<1296:AIAFGG>2.0.CO;2.

Inoue, K., and L. Back, 2015: Column-integrated moist static energy budget analysis on various time scales during TOGA COARE. *J. Atmos. Sci.*, **72**, 1856–1871, https://doi.org/10.1175/JAS-D-14-0249.1.

——, Á. F. Adames, and K. Yasunaga, 2020: Vertical velocity profiles in convectively coupled equatorial waves and MJO: New diagnoses of vertical velocity profiles in the wavenumber–frequency domain. *J. Atmos. Sci.*, **77**, 2139–2162, https://doi.org/10.1175/JAS-D-19-0209.1.

Jiang, X., M. Zhao, E. D. Maloney, and D. E. Waliser, 2016: Convective moisture adjustment time scale as a key factor in regulating model amplitude of the Madden-Julian oscillation. *Geophys. Res. Lett.*, **43**, 10 412–10 419, https://doi.org/10.1002/2016GL070898.

Kiladis, G. N., K. H. Straub, and P. T. Haertel, 2005: Zonal and vertical structure of the Madden–Julian oscillation. *J. Atmos. Sci.*, **62**, 2790–2809, https://doi.org/10.1175/JAS3520.1.

——, C. D. Thorncroft, and N. M. J. Hall, 2006: Three-dimensional structure and dynamics of African easterly waves. Part I: Observations. *J. Atmos. Sci.*, **63**, 2212–2230, https://doi.org/10.1175/JAS3741.1.

——, M. C. Wheeler, P. T. Haertel, K. H. Straub, and P. E. Roundy, 2009: Convectively coupled equatorial waves. *Rev. Geophys.*, **47**, RG2003, https://doi.org/10.1029/2008RG000266.

——, J. Dias, and M. Gehne, 2016: The relationship between equatorial mixed Rossby–gravity and eastward inertio-gravity waves. Part I. *J. Atmos. Sci.*, **73**, 2123–2145, https://doi.org/10.1175/JAS-D-15-0230.1.

Kim, D., J.-S. Kug, and A. H. Sobel, 2014: Propagating versus nonpropagating Madden–Julian oscillation events. *J. Climate*, **27**, 111–125, https://doi.org/10.1175/JCLI-D-13-00084.1.

Kiranmayi, L., and E. D. Maloney, 2011: Intraseasonal moist static energy budget in reanalysis data. *J. Geophys. Res.*, **116**, D21117, https://doi.org/10.1029/2011JD016031.

Liebmann, B., G. N. Kiladis, L. M. V. Carvalho, C. Jones, C. S. Vera, I. Bladé, and D. Allured, 2009: Origin of convectively coupled kelvin waves over South America. *J. Climate*, **22**, 300–315, https://doi.org/10.1175/2008JCLI2340.1.

Livezey, R. E., and W. Y. Chen, 1983: Statistical field significance and its determination by Monte Carlo techniques. *Mon. Wea. Rev.*, **111**, 46–59, https://doi.org/10.1175/1520-0493(1983)111<0046:SFSAID>2.0.CO;2.

Maloney, E. D., 2009: The moist static energy budget of a composite tropical intraseasonal oscillation in a climate model. *J. Climate*, **22**, 711–729, https://doi.org/10.1175/2008JCLI2542.1.

Mapes, B., S. Tulich, J. Lin, and P. Zuidema, 2006: The mesoscale convection life cycle: Building block or prototype for large-scale tropical waves? *Dyn. Atmos. Oceans*, **42**, 3–29, https://doi.org/10.1016/j.dynatmoce.2006.03.003.

Martin, S. T., and Coauthors, 2016: Introduction: Observations and modeling of the Green Ocean Amazon (GoAmazon2014/5). *Atmos. Chem. Phys.*, **16**, 4785–4797, https://doi.org/10.5194/acp-16-4785-2016.

Matsuno, T., 1966: Quasi-geostrophic motions in the equatorial area. *J. Meteor. Soc. Japan*, **44**, 25–43, https://doi.org/10.2151/jmsj1965.44.1_25.

Matthews, A. J., 2000: Propagation mechanisms for the Madden-Julian oscillation. *Quart. J. Roy. Meteor. Soc.*, **126**, 2637–2651, https://doi.org/10.1002/qj.49712656902.

Mayta, V. C., and A. F. Adames, 2021: Two-day westward-propagating inertio-gravity waves during GoAmazon. *J. Atmos. Sci.*, **78**, 3727–3743, https://doi.org/10.1175/JAS-D-20-0358.1.

——, T. Ambrizzi, J. C. Espinoza, and P. L. Silva Dias, 2019: The role of the Madden-Julian oscillation on the Amazon basin intraseasonal rainfall variability. *Int. J. Climatol.*, **39**, 343–360, https://doi.org/10.1002/joc.5810.

——, N. P. Silva, T. Ambrizzi, P. L. S. Dias, and J. C. Espinoza, 2020: Assessing the skill of all-season diverse Madden-Julian oscillation indices for the intraseasonal Amazon precipitation. *Climate Dyn.*, **54**, 3729–3749, https://doi.org/10.1007/s00382-020-05202-9.

——, G. N. Kiladis, J. Dias, P. L. S. Dias, and M. Gehne, 2021: Convectively coupled Kelvin waves over tropical South America. *J. Climate*, **34**, 6531–6547, https://doi.org/10.1175/JCLI-D-20-0662.1.

——, Á. F. Adames, and F. Ahmed, 2022: Westward-propagating moisture mode over the tropical Western Hemisphere. *Geophys. Res. Lett.*, **49**, e2022GL097799, https://doi.org/10.1029/2022GL097799.

Neelin, J. D., 2007: Moist dynamics of tropical convection zones in monsoons, teleconnections, and global warming. *The Global Circulation of the Atmosphere*, A. H. Sobel and T. Schneider, Eds., Princeton University Press, 267–301.

——, and I. M. Held, 1987: Modeling tropical convergence based on the moist static energy budget. *Mon. Wea. Rev.*, **115**, 3–12, https://doi.org/10.1175/1520-0493(1987)115<0003:MTCBOT>2.0.CO;2.

Nogués-Paegle, J., and K. C. Mo, 1997: Alternating wet and dry conditions over South America during summer. *Mon. Wea. Rev.*, **125**, 279–291, https://doi.org/10.1175/1520-0493(1997)125<0279:AWADCO>2.0.CO;2.

North, G. R., T. L. Bell, R. F. Cahalan, and F. J. Moeng, 1982: Sampling errors in the estimation of empirical orthogonal functions. *Mon. Wea. Rev.*, **110**, 699–706, https://doi.org/10.1175/1520-0493(1982)110<0699:SEITEO>2.0.CO;2.

Powell, S. W., 2017: Successive MJO propagation in MERRA-2 reanalysis. *Geophys. Res. Lett.*, **44**, 5178–5186, https://doi.org/10.1002/2017GL073399.

Randall, D., 2015: *An Introduction to the Global Circulation of the Atmosphere*. Princeton University Press, 456 pp.

Raymond, D. J., 2001: A new model of the Madden–Julian oscillation. *J. Atmos. Sci.*, **58**, 2807–2819, https://doi.org/10.1175/1520-0469(2001)058<2807:ANMOTM>2.0.CO;2.

——, S. L. Sessions, A. H. Sobel, and Z. Fuchs, 2009: The mechanics of gross moist stability. *J. Adv. Model. Earth Syst.*, **1**, https://doi.org/10.3894/JAMES.2009.1.9.

Ren, P., D. Kim, M.-S. Ahn, D. Kang, and H.-L. Ren, 2021: Intercomparison of MJO column moist static energy and water vapor budget among six modern reanalysis products. *J. Climate*, **34**, 2977–3001, https://doi.org/10.1175/JCLI-D-20-0653.1.

Serra, Y. L., G. N. Kiladis, and K. I. Hodges, 2010: Tracking and mean structure of easterly waves over the Intra-Americas Sea. *J. Climate*, **23**, 4823–4840, https://doi.org/10.1175/2010JCLI3223.1.

——, A. Rowe, D. K. Adams, and G. N. Kiladis, 2020: Kelvin waves during GOAmazon and their relationship to deep convection. *J. Atmos. Sci.*, **77**, 3533–3550, https://doi.org/10.1175/JAS-D-20-0008.1.

Silva Dias, M. A. F., and R. N. Ferreira, 1992: Application of a linear spectral model to the study of Amazonian squall lines during GTE/ABLE 2B. *J. Geophys. Res.*, **97**, 20 405–20 419, https://doi.org/10.1029/92JD01333.

Snide, C. E., A. F. Adames, S. W. Powell, and V. C. Mayta, 2022: The role of large-scale moistening by adiabatic lifting in the Madden–Julian oscillation convective onset. *J. Climate*, **35**, 269–284, https://doi.org/10.1175/JCLI-D-21-0322.1.

Sobel, A., and E. Maloney, 2012: An idealized semi-empirical framework for modeling the Madden–Julian oscillation. *J. Atmos. Sci.*, **69**, 1691–1705, https://doi.org/10.1175/JAS-D-11-0118.1.

——, S. E. Yuter, C. S. Bretherton, and G. N. Kiladis, 2004: Large-scale meteorology and deep convection during TRMM KWAJEX. *Mon. Wea. Rev.*, **132**, 422–444, https://doi.org/10.1175/1520-0493(2004)132<0422:LMADCD>2.0.CO;2.

——, S. Wang, and D. Kim, 2014: Moist static energy budget of the MJO during DYNAMO. *J. Atmos. Sci.*, **71**, 4276–4291, https://doi.org/10.1175/JAS-D-14-0052.1.

Straub, K. H., and G. N. Kiladis, 2002: Observations of a convectively coupled Kelvin wave in the eastern Pacific ITCZ. *J. Atmos. Sci.*, **59**, 30–53, https://doi.org/10.1175/1520-0469(2002)059<0030:OOACCK>2.0.CO;2.

Sumi, Y., and H. Masunaga, 2016: A moist static energy budget analysis of quasi-2-day waves using satellite and reanalysis data. *J. Atmos. Sci.*, **73**, 743–759, https://doi.org/10.1175/JAS-D-15-0098.1.

Takayabu, Y. N., 1994: Large-scale cloud disturbances associated with equatorial waves. *J. Meteor. Soc. Japan*, **72**, 433–449, https://doi.org/10.2151/jmsj1965.72.3_433.

——, K.-M. Lau, and C.-H. Sui, 1996: Observation of a quasi-2-day wave during TOGA COARE. *Mon. Wea. Rev.*, **124**, 1892–1913, https://doi.org/10.1175/1520-0493(1996)124<1892:OOAQDW>2.0.CO;2.

Tang, S., and Coauthors, 2016: Large-scale vertical velocity, diabatic heating and drying profiles associated with seasonal and diurnal variations of convective systems observed in the GoAmazon2014/5 experiment. *Atmos. Chem. Phys.*, **16**, 14 249–14 264, https://doi.org/10.5194/acp-16-14249-2016.

Vera, C. S., M. S. Alvarez, P. L. M. Gonzalez, B. Liebmann, and G. N. Kiladis, 2018: Seasonal cycle of precipitation variability in South America on intraseasonal timescales. *Climate Dyn.*, **51**, 1991–2001, https://doi.org/10.1007/s00382-017-3994-1.

Wheeler, M., and G. N. Kiladis, 1999: Convectively coupled equatorial waves: Analysis of clouds in the wavenumber–frequency domain. *J. Atmos. Sci.*, **56**, 374–399, https://doi.org/10.1175/1520-0469(1999)056<0374:CCEWAO>2.0.CO;2.

——, ——, and P. J. Webster, 2000: Large-scale dynamical fields associated with convectively coupled equatorial waves. *J. Atmos. Sci.*, **57**, 613–640, https://doi.org/10.1175/1520-0469(2000)057<0613:LSDFAW>2.0.CO;2.

Wolding, B., J. Dias, G. Kiladis, E. Maloney, and M. Branson, 2020: Interactions between moisture and tropical convection. Part II: The convective coupling of equatorial waves. *J. Atmos. Sci.*, **77**, 1801–1819, https://doi.org/10.1175/JAS-D-19-0226.1.

——, S. W. Powell, F. Ahmed, J. Dias, M. Gehne, G. Kiladis, and J. D. Neelin, 2022: Tropical thermodynamic-convection coupling in observations and reanalyses. *J. Atmos. Sci.*, **79**, 1781–1803, https://doi.org/10.1175/JAS-D-21-0256.1.

Yanai, M., S. Esbensen, and J.-H. Chu, 1973: Determination of bulk properties of tropical cloud clusters from large-scale heat and moisture budgets. *J. Atmos. Sci.*, **30**, 611–627, https://doi.org/10.1175/1520-0469(1973)030<0611:DOBPOT>2.0.CO;2.

Yang, G.-Y., B. Hoskins, and J. Slingo, 2007: Convectively coupled equatorial waves. Part I: Horizontal and vertical structures. *J. Atmos. Sci.*, **64**, 3406–3423, https://doi.org/10.1175/JAS4017.1.

Yasunaga, K., S. Yokoi, K. Inoue, and B. E. Mapes, 2019: Space–time spectral analysis of the moist static energy budget equation. *J. Climate*, **32**, 501–529, https://doi.org/10.1175/JCLI-D-18-0334.1.

Zhang, C., Á. F. Adames, B. Khouider, B. Wang, and D. Yang, 2020: Four theories of the Madden-Julian oscillation. *Rev. Geophys.*, **58**, e2019RG000685, https://doi.org/10.1029/2019RG000685.

Zhang, M. H., and J. L. Lin, 1997: Constrained variational analysis of sounding data based on column-integrated budgets of mass, heat, moisture, and momentum: Approach and application to ARM measurements. *J. Atmos. Sci.*, **54**, 1503–1524, https://doi.org/10.1175/1520-0469(1997)054<1503:CVAOSD>2.0.CO;2.